



This is a repository copy of *Efficacy Dependence of Photodynamic Therapy Mediated by Upconversion Nanoparticles: Subcellular Positioning and Irradiation Productivity*.

White Rose Research Online URL for this paper:
<http://eprints.whiterose.ac.uk/114888/>

Version: Accepted Version

Article:

Chen, D., Tao, R., Tao, K. et al. (6 more authors) (2017) Efficacy Dependence of Photodynamic Therapy Mediated by Upconversion Nanoparticles: Subcellular Positioning and Irradiation Productivity. *Small*, 13 (13). 1602053. ISSN 1613-6810

<https://doi.org/10.1002/smll.201602053>

This is the peer reviewed version of the following article: D. Chen, R. Tao, K. Tao, B. Chen, S. K. Choi, Q. Tian, Y. Xu, G. Zhou, K. Sun, *Small* 2017, 13, 1602053, which has been published in final form at <http://doi.org/10.1002/smll.201602053>. This article may be used for non-commercial purposes in accordance with Wiley Terms and Conditions for Self-Archiving.

Reuse

Unless indicated otherwise, fulltext items are protected by copyright with all rights reserved. The copyright exception in section 29 of the Copyright, Designs and Patents Act 1988 allows the making of a single copy solely for the purpose of non-commercial research or private study within the limits of fair dealing. The publisher or other rights-holder may allow further reproduction and re-use of this version - refer to the White Rose Research Online record for this item. Where records identify the publisher as the copyright holder, users can verify any specific terms of use on the publisher's website.

Takedown

If you consider content in White Rose Research Online to be in breach of UK law, please notify us by emailing eprints@whiterose.ac.uk including the URL of the record and the reason for the withdrawal request.



eprints@whiterose.ac.uk
<https://eprints.whiterose.ac.uk/>

DOI: 10.1002/smll.201602053

Article type: Full Paper

Efficacy dependence of photodynamic therapy mediated by upconversion nanoparticles: subcellular positioning and irradiation productivity

Dexin Chen†, Ran Tao†, Ke Tao, Biqiong Chen, Seok Ki Choi, Qing Tian, Yawen Xu, Guangdong Zhou*, Kang Sun**

D. Chen, Dr. K Tao, Q. Tian, Prof. K. Sun,
State Key Lab of Metal Matrix Composites,
Shanghai Jiao Tong University, Shanghai 200240, P. R. China
E-mail: ktao@sjtu.edu.cn, ksun@sjtu.edu.cn

R. Tao,
Department of Plastic Surgery,
Changhai Hospital, Second Military Medical University, Shanghai 200433, P. R. China

Y. Xu, Prof. G. Zhou,
Department of Plastic and Reconstructive Surgery, Shanghai 9th People's Hospital, Shanghai
Jiao Tong University School of Medicine, Shanghai Key Laboratory of Tissue Engineering,
Shanghai Stem Cell Institute, Shanghai, P. R. China

E-mail: guangdongzhou@126.com

Dr. B. Chen,
Department of Materials Science and Engineering, University of Sheffield, Mappin Street,
Sheffield, S1 3JD, United Kingdom

Dr. S. K. Choi,
Michigan Nanotechnology Institute for Medicine and Biological Sciences, and Department of
Internal Medicine, University of Michigan, Ann Arbor, Michigan 48109, United States

Keywords: Photodynamic, upconversion nanoparticles, reactive oxygen species, subcellular targeting

Abstract.

Singlet oxygen ($^1\text{O}_2$), as an important kind of reactive oxygen species (ROS) and main therapeutic agent in photodynamic therapy (PDT), only have a half-life of 40 ns and an effective radius of 20 nm, which cause significant obstacles for improving PDT efficacy. In this work, we developed novel upconversion nanoparticle (UCN)-based nanoplatfroms with a minimized distance between UCNs and a photosensitizer, protoporphyrin IX (PpIX), and a controllable payload of PpIX, to enhance and control ROS production. The ability of the nanoplatfrom to target different subcellular organelles such as cell membrane and mitochondria was demonstrated via surface modification of the nanoplatfrom with different

targeting ligands. The results showed that the mitochondria-targeting nanoplatfoms resulted in significantly increased capability of both tumor cell-killing and inhibition of tumor growth. Subcellular targeting of nanoparticles leads to the death of cancer cells in different manners. However, the efficiency of ROS generation almost had no influence on the tumor cell viability during the period of evaluation. These findings suggest that specific subcellular targeting of the nanoplatfoms enhances the PDT efficacy more effectively than the increase of ROS production, and may shed light on future novel designs of effective and controllable PDT nanoplatfoms.

1. Introduction

Photodynamic therapy (PDT) is a tumor-ablative oncologic intervention that involves the excitation of photosensitizer (PS) molecules with light of a specific wavelength^[1,2] to produce cytotoxic reactive oxygen species (ROS) for irreversibly damaging tumor cells^[3]. Its merits are minimal invasiveness and low side effects. However, the challenges are to ablate tumor tissues with high efficiency, including limited penetrating depths, low ROS production efficiency, short half-lives and effective radii of singlet oxygen ($^1\text{O}_2$), the most effective kind of ROS^[4,5]. As an emerging platform in the field of PDT, upconversion nanoparticles (UCNs) serving as a PS carrier have attracted intensive attention in recent years^[6,7]. Upon near-infrared (NIR) light excitation, UCNs are able to emit visible or ultraviolet light with controllable wavelengths, which could match the absorption wavelength of the loaded photosensitizer, and therefore play as a transducer. Given the deep tissue penetration capability of NIR light^[8], NIR-excited UCNs can be located in in-depth tissues to activate loaded PS molecules for PDT treatment.

In the past decade, various strategies to load PS molecules onto UCNs have been designed for improving PDT efficacy, mainly in terms of optimization of ROS production^[9-16]. One of the

strategies was to improve the match between the wavelength bands of UCN emission and PS absorption. For example, Chen et. al.^[9] chose methylene blue as the photosensitizer which had a mismatch of <5 nm between its absorption wavelength and the emission wavelength of UCNs. Idris et. al.^[10] simultaneously conjugated a type of UCNs with two different PS molecules, in which the absorption peak of each PS molecule matched well with one of the major emission peaks of UCNs for efficient energy transfer and absorption. However, these optimized methods were still not sufficient to regress tumor cells completely^[10]. Other strategies were also designed to elevate the loading capacity of the photosensitizer in order to increase ROS production. For example, Cui et al.^[11] developed amphiphilic chitosan modified UCNs with a PS loading capacity of up to ~10%, resulting in inhibiting 66 wt% tumor growth as compared to the blank control. However, in these approaches, a coating layer of silica or polymer with a thickness generally greater than 10 nm^[9-15] was demanded for sufficient PS loading. Owing to the fact that ROS production is an energy transfer process, a thicker layer of PS loading, which means the increased distance between PS molecules and UCNs, will largely reduce the efficiency of energy transfer. Furthermore, the increased production of ROS arising from the increasing concentration of nanocarriers^[14,16] may also lead to the risks of toxicity. Thus, it is worth developing novel strategies to improve the extent of tumor regression via the increase of PDT efficacy.

Because of the short half-life and effective radius of $^1\text{O}_2$, the dominant kind of ROS^[5,17], the effective area to damage tumor cells is limited to the neighborhood of the nanoplateforms in subcellular scale. Meanwhile, each therapeutic agent has an optimal mechanism of action, which usually occurs primarily in a specific subcellular organelle in order to initiate precise inhibition or apoptosis of a cancer cell^[18-20]. For example, pro-apoptotic drugs have primary effect on mitochondrial membrane^[21], and oligonucleotides for gene therapy must home in the cytosol and nucleus^[22,23]. Previous results from the delivery of classical drugs to specific

organelles revealed that the therapeutic efficacy was several-fold greater than that of non-targeted drugs through modification with liposome^[24], dendrimer^[25], or polymeric carriers^[26-29]; those non-targeted drugs were uncontrolledly released under the disintegration of liposomes or the degradation of polymeric carriers. Therefore, it is reasonable to hypothesize that UCN-based PDT nanoplatfoms targeting to particular subcellular organelles can precisely generate $^1\text{O}_2$ within the effective location to kill tumor cells, and can be spatiotemporally controllable since the NIR light can trigger $^1\text{O}_2$ generation in an immediate and sensitive manner^[30-32].

Furthermore, direct experimental results concerning the dose effect of ROS on PDT efficacy have not been reported in the literature despite that ROS is the therapeutic agent in photodynamic therapy. Photosensitizers can continuously produce ROS so long as it is under the illumination of an appropriate light with a continuous oxygen supply^[30, 32-34], meaning that a sufficient amount of ROS can be generated even by a nanocarrier with a low loading of a photosensitizer under a prolonged illumination. Yet, it remains unclear whether the amount of ROS produced under a relatively long irradiation time is sufficient for efficient PDT therapy.

To address the above issues, we aimed to identify the crucial factors that can improve the PDT efficacy effectively by increasing ROS production and targeting ROS production at the subcellular position. Nanoplatfoms, based on UCN as a light transducer and protoporphyrin IX (PpIX) as the ROS producer, with novel features were designed. To investigate the effect of ROS production on PDT efficacy, 1) a thinner PpIX-loaded layer (3~5 nm) outside UCN nanoparticles was designed to improve the efficiency of energy transfer between UCN core and PpIX molecules; and 2) a controllable payload of PpIX was applied to adjust the efficiency of ROS generation. To study the impact of subcellular positioning on PDT efficacy, different pertinent targeting ligands were covalently bonded onto the nanoplatfom to target

different subcellular organelles. The PDT efficacy of novel nanoplatfoms were characterized through both *in vitro* and *in vivo* studies. The effect of irradiation time on the PDT therapy was also investigated.

2. Results

2.1. UCN based PDT nanoplatfoms with a 3-5 nm silica coating layer

Two approaches for loading PpIX in a 3~5 nm silica layer were conducted in this work, together with a control method that produced a ~15 nm coating. The thin silica outside nanoparticles, as a close UCN-PpIX proximity for energy transfer, was successfully prepared by a modified reverse microemulsion approach^[16,34], as shown in **Figure 1**. Notable features of the modified method include: firstly, the addition of a small amount of dimethyl sulfoxide (DMSO) into the water phase of the emulsion, which increases the solubility of PpIX in the water phase and therefore improves its dispersion; secondly, an aminopropyltriethoxysilane agent was used as a silica precursor for making the thin coating layer (denoted as sample APTS). Meanwhile a novel synthetic method was also designed in which PpIX was first covalently conjugated with aminopropyltriethoxysilane (see Supporting information)^[35]. The conjugation was then used as a coating precursor. The latter method allowed us to adjust the loading amount of PpIX and the resultant nanoplatfoms were labeled as sample CovX (X = 1, 1.5, 3, 6, each number indicative of a different amount of PpIX feeding, see **Figure 1**). We also prepared the control samples by coating UCNs with tetraethylorthosilicate as a silica precursor (denoted as sample TEOS). TEM images of silica coated UCNs are shown in **Figure 1**. UCNs show monodispersion with a size of ~40 nm in diameter before coating. Using aminopropyltriethoxysilane as the precursor successfully limited the thickness of the outer coating layer to ~3.0 nm. Similarly, a coating layer by use of silane covalently bonded with PpIX has only about 3~5 nm in thickness. However, coating of a tetraethylorthosilicate-based layer led to a ~15 nm increase in thickness of the outer layer.

2.2. Controlled and increased ROS producing efficacy

The amount of PpIX incorporated in the coating layer was determined by comparing UV–Vis absorption measured at 410 nm to a standard concentration-absorption curve. A blank sample of only silica coated UCNs was regarded as a control without any absorption at 410 nm in the UV-Vis curve. This indicates that addition of silica has no interference on the UV–Vis absorption of UCNs. The results are shown in the table of **Figure 1**. Under the same amount of PpIX added, use of aminopropyltriethoxysilane led to ~1.12% PpIX incorporated in the coating layer, lower than the tetraethylorthosilicate of ~1.70%. In contrast, with PpIX pre-attached to aminopropyltriethoxysilane as precursor, the loading amounts of PpIX incorporated in the coating layer vary significantly from ~0.46% (Cov1) to ~3.26% (Cov6). Since the feeding doses of PpIX in samples TEOS and APTS are the same as that of Cov6, it can be concluded that the PpIX-silane precursor for sample Cov6 results in an enhanced loading amount of PS molecules (~3.26%) compared to those of TEOS (~1.70%) and APTS (~1.12%).

The influence of coating layer thickness on the steady state energy transfer efficiency between UCNs and PpIX was evaluated by measuring the fluorescent intensity of drug-loaded UCNs^[36]. As shown in the table of **Figure 1**, all ‘Cov’ samples have the energy transfer efficiency in the range of 32~85% with an outer layer of 3~5 nm in thickness. In contrast, sample TEOS with a 15 nm-thick outer layer has drastically lower energy transfer efficiency, 13.6%, despite of a higher amount of PpIX incorporated in the coating layer than Cov1 and Cov 1.5. Meanwhile, the transient state energy transfer efficiency was measured by the luminescence decay lifetime^[36]. The results showed that the decay time of 540 nm emission of UCNs coating with a 3-5nm SiO₂ was significantly shortened after loading with PpIX, while that of 660nm almost kept the same (shown in **Figure S3**). Accordingly, the energy transfer

efficiency was about 42.9%, 41.1%, and 13.6% for the sample Cov3, APTS, and TEOS, respectively.

The capability of the nanoplateforms to generate ROS was investigated by using a chemical method with 1,3-diphenylisobenzofuran (DPBF) as an acceptor of ROS generated. In this assay, the reaction of DPBF with ROS results in the decay of its absorption intensity of DPBF in UV-Vis curve. Such a spectral change of DPBF in UV-Vis curve allows us to determine the concentration of ROS produced from different UCN hybrid samples^[37]. Under 980 nm laser irradiation, the absorption intensity of DPBF at about 400 nm decreased gradually with time in all samples (as shown in **Figure S4**), from which time-dependent curves of ROS generation can be determined. As shown in **Figure 2a**, under the same NIR laser excitation, sample Cov6 possesses the highest ROS generation efficiency, followed by samples Cov3, APTS, Cov1.5, consequently, and samples Cov1 and TEOS show the lowest. Obviously, with a coating layer of the same thickness of 3~5 nm, the higher the loading amount of PpIX incorporated in the coating layer is, the higher the ROS generation efficiency will be. Based on the results of samples APTS and Cov3 with almost the same amount of PpIX, the ROS generation efficiency is barely influenced by the covalent bonding between PpIX and aminopropyltriethoxysilane. However, the ROS generation efficiency of sample Cov3 with the thickness of 3~5 nm is much higher than sample TEOS with the coating thickness of ~15 nm, although the loading of PpIX on Cov3 is slightly less than TEOS. This observation clearly suggests that PpIX loading in the thinner coating layer leads to higher ROS generating efficiency due to a shorter distance between photosensitizer molecules and UCNs.

As $^1\text{O}_2$ is the main executive part with short half-life in ROS, we further determining the generation of $^1\text{O}_2$ by using 9,10-anthracenediyl-bis(methylene) dimalonic acid (ABMDMA) as the indicator, owing to that the absorbance of ABMDMA in visible range can be decayed

by $^1\text{O}_2$ ^[38,39]. We found that the UV-Vis spectra of samples were gradually quenched with prolonging irradiation time, as shown in **Figure S5**. Meanwhile the dose of produced $^1\text{O}_2$ (**Figure 2b**) showed a similar regularity with the results of ROS generation. The results demonstrated the effective production of $^1\text{O}_2$ by the presented nanoplatfroms, and the dose of $^1\text{O}_2$ could be varied with controlling the thickness of coating layer and loading amount of PS.

2.3. Subcellular targeting via surface modification

Due to the availability of the amine group originated from aminopropyltriethoxysilane, a NH_2/COOH coupling reaction can be used to conjugate certain targeting ligands onto the nanoplatfroms. In our case, folic acid (FA)^[37,40] and (3-carboxypropyl) triphenylphosphonium bromide (TPP)^[41,42] were conjugated onto the surface of nanoparticles respectively (as shown in **Figure 3a**). The cellular uptake of surface modified UCNs-PpIX nanoparticles was observed using a two-photon fluorescence confocal microscope, which is equipped with a 980 nm pulse laser resource. **Figure 3a** shows images of HeLa cells associated with each of these UCNs-PpIX nanoparticles in which nuclei are detected by 4',6-diamidino-2-phenylindole (DAPI) staining. Each of the UCN-PpIX nanoparticles, stained with DAPI, shows green luminescence at the location close to a cell nucleus. Compared to unmodified UCN-PpIX nanoparticles, the modification with FA or TPP significantly increased the cellular uptake amount of UCNs. For quantitative analysis, the amounts of UCN-PpIX nanoparticles were determined by using inductively coupled plasma-atomic emission spectroscopy (ICP-AES) as summarized in **Figure 3b**. The results showed the surface modification with either FA or TPP ligand increased the cellular uptake amount of UCNs-PpIX nanoparticles by up to ~6 times higher than unmodified UCNs-PpIX nanoparticles, confirming the cell imaging results. Without surface modification, the difference in cellular uptake was ~2.5-fold between APTS and Cov6. However, samples APTS and Cov6 with FA or TPP modification have similar amounts of cellular uptake. Transmission electron microscopy (TEM) was employed to

observe the subcellular locations of the above nanoparticles. **Figure 4** shows TEM images of HeLa cells incubated with Cov6 samples with different surface modifications. It is clearly visible that most of the UCNs-PpIX nanoparticles modified with FA are located near the cell membrane. In contrast, the UCNs-PpIX nanoparticles modified with TPP were mainly found near mitochondria.

To further identify mitochondria targeting of TPP modified nanoparticles, Rhodamine 123 (Rh123) was used to specifically stain the mitochondria of HeLa cells internalized with Cov6-TPP and Cov6-FA, respectively, while a control experiment without nanoparticles was performed. The images of control group indicated the successful staining of DAPI and Rh123 (as shown in **Figure 5**). For the experimental groups, we directly observed the fluorescence of PpIX ($\lambda_{\text{ex}}=552\text{nm}$, $\lambda_{\text{em}}=700\text{nm}$) loaded on UCNs. The results showed that for the sample Cov6-FA, the fluorescence from PpIX and Rh123 are almost separated. In contrast, the fluorescence from PpIX in sample Cov6-TPP are almost covered by Rh123, indicating a efficient delivery to mitochondria. For statistically analyzing the targeting efficiency, a Pearson's correlation coefficient that identify colocalization of the fluorescence from Rh123 and PpIX was calculated with an imaging analysis software ImageJ[®], based on about 2000 cells for each sample. Pearson's correlation coefficient is one of the standard procedures in pattern recognition for matching one image with another and can be used to describe the degree of overlap between two patterns.^[43] Our result showed that Pearson Coefficient for the sample Cov6-TPP is 0.817 ± 0.029 , while for the sample Cov6-FA it is 0.567 ± 0.064 , which indicates that the modification of TPP tailors more nanoparticles to the sites near mitochondria.

2.4. *In vitro* studies on the influence of ROS generation, irradiation time and nanoparticle position

To study the influence of nanoparticle position on PDT efficacy, we first evaluated all the unmodified samples in a control experiment. Without 980 nm irradiation, HeLa cells incubated with all the unmodified samples were alive and their viability generally remained almost 100% (**Figure 6**, blue bars). Upon irradiation for 15 min (**Figure 6**, pink bars), the viability of HeLa cells incubated with all the unmodified samples decreased to the range of 60–70%, which implies death of some HeLa cells. Although the difference in the cellular uptake between unmodified APTS and unmodified Cov6 was ~2.5 times, there was almost no significant difference between cell viabilities of both samples. This enlightens that the uptake amount of nanoparticles is not the only factor influencing the viability of HeLa cells. Furthermore, we performed the same evaluation experiment of cell viability without washing after incubation with all the unmodified samples to maintain the same total amounts of nanoparticles. Under the same condition of irradiation for 15 min, the average cell viabilities for all the unwashed samples were only slightly further decreased (**Figure 6**, green bars). Again, this implies that cell-killing efficacy is more relevant to the subcellular location of nanoparticles rather than the total dose.

The effect of the subcellular locations of UCNs-PpIX nanoparticles on the cell viability was measured by Cov6 samples with and without ligand modification. As shown in **Figure 7**, without NIR irradiation, there is no apparent decrease in cell viabilities and no difference for all samples. After NIR irradiation for 10 min, the cell viability of HeLa cells incubated with FA-modified Cov6 (located near cell membrane) is ~15% lower than treated with unmodified Cov6 (67%~70%). Furthermore, cell viability of HeLa cells incubated with TPP-modified Cov6 (located near mitochondria) significantly decreased to ~40%, much lower than the sample FA-modified Cov6. As discussed earlier, the cellular uptake amount of Cov6-TPP is only slightly lower than that of Cov6-FA (**Figure 3b**). Therefore, these results imply that

locating UCNs-PpIX nanoparticles at certain subcellular position, such as mitochondria, is more effective for improving PDT efficacy.

Figure 7 also showed that the effect of irradiation time on the cell viability of each Cov6 sample. The results showed that irradiation within 30 min leads to almost the same viability of cells for all samples. However, prolongation of exposure time above 30 min results in a further decrease in the viability of HeLa cells for all the three kinds of surface modified samples. With the same FA modification shown in **Figure 8**, the cell viabilities of samples APTS, Cov1.5 and Cov6 experienced almost the same decreases during the same periods of NIR irradiation. Samples APTS and Cov6 modified with different ligands were also compared (**Figure 9**). The results showed no significant statistical difference between APTS and Cov6 under the same NIR irradiation time. As shown in **Figure 2**, the ROS generation of Cov6 is about 3-fold higher than samples APTS and Cov1.5. Therefore, the above results indicate that there is no direct correlation between the cell viability and the amount of ROS generation.

Fluorescence-activated cell sorting (FACS) technique allows us to investigate the mechanisms underlying the cytotoxicity of nanoparticles such as the extent of DNA damage^[44]. The FACS results for both two Cov6 samples (**Figure 10**) showed that the number of cells positively stained by Annexin V and/or propidium iodine (PI) increased after 15 min irradiation, demonstrating the death of cells. When the irradiation time was prolonged to 60 min, treatment with FA-modified Cov6 led to the significant increase of cells only positively stained by PI, indicating that the membrane integrity of cells was destroyed in this case. In contrast, TPP-modified Cov6 sample significantly results in the location of both Annexin V and PI double stained, indicating the necrosis and late stage apoptosis of HeLa cells with an integrated membrane. All these experimental results were consistently reproducible.

2.5. *In vivo* studies on the influence of nanoparticle position

The PDT efficacy of nanoparticles with different surface modifications was further investigated on tumor-bearing mouse model with $n=6$ for each group. For the groups with injected UCNs-PpIX nanoparticles under irradiation of NIR laser, green light emitted from *in vivo* nanoparticles can be clearly observed by naked eyes (**Figure 11a**), indicating the successful NIR penetration through living body for its potential in simultaneous NIR fluorescent imaging and PDT. As shown in **Figure 11** (b and c), the tumors in the two control groups without UCNs-PpIX nanoparticles kept on growing to a ~2.6-fold volume in 11 days, indicating that NIR light alone has no effect on the growth of the tumor tissue. On the contrary, NIR irradiation together with injection of Cov6-FA and Cov6-TPP significantly inhibited the tumor growth in spite of the irradiation only performed for an hour in the first 2 days. Especially, Cov6-TPP nanoparticles under NIR irradiation show stronger ability of inhibiting tumor growth than that of Cov6-FA during the whole period of *in vivo* experiment. This result clearly suggests that TPP modified nanoparticles near mitochondria exert much higher PDT efficacy than FA modified ones near cell membrane.

The histological results from tumor-bearing mouse model were shown in **Figure 12**. The morphology, size and staining of the tumor cells in control groups (whether with or without laser irradiation) are at variance, indicating the continuous growth of tumor cells without nanoparticles. Meanwhile, after injection of nanoparticles, the tumor still kept growing without NIR irradiation. In contrast, markedly increased death of cells was observed after irradiation, as obvious blank or unstained areas can be observed. Interestingly, green fluorescence emitted from Cov6-TPP groups (with or without laser) 12 days after injection, and the illuminating positions overlay the areas of apoptotic/necrotic tumor cells. On the contrary, the fluorescence of UCNs cannot be observed for the cell membrane targeted Cov6-FA sample, which may suggest that the membrane-targeting mode easily results in the

metabolism. This result indicated that the nanoparticles with the mitochondria targeting behavior could also be applicable for both long-term therapy and long-term fluorescent imaging.

3. Discussion

This work modified a classical synthetic process to coat the outer layer of silica by using aminopropyltriethoxysilane (or PpIX conjugated aminopropyltriethoxysilane) as a precursor, and the thickness of the coating layer can be restricted in ~3 nm. As we know, the efficiency of ROS production is based on the energy transfer between UCNs as a donor and PS molecules as an acceptor which is inversely proportional to the sixth power of the distance between the donor and acceptor pair^[45,46]. Therefore, the thickness of the coating layer outside UCNs is significantly related to the ROS generation efficiency. Our results showed that, compared to sample TEOS with a coating layer of ~15 nm in thickness, which is comparable to the references^[9-16], all the samples with a coating layer of ~3 nm in thickness had much higher energy transfer efficiency between PpIX and UCNs for enhancing ROS generation efficiency. Meanwhile the covalent bond between PpIX and aminopropyltriethoxysilane enables the control of the amount of PpIX loading within the thin silica layer, which resulted in the controllability of ROS production.

Another advance for current coating protocol is that the -NH₂ from aminopropyltriethoxysilane presented on the surface provide further surface modification capabilities for subcellular localization. FA is one of the well-established ligands for targeting certain types of cancer cell including HeLa cells in current work because folate receptors in such cells are significantly upregulated compared to normal healthy cells^[37,40]. In this paper, FA-modified UCNs-PpIX nanoparticles are mostly located near the cellular membrane instead of lysosome or endosome shown in the literature^[37,40]. This is possibly owing to the multivalent FA receptor association of FA-modified UCNs-PpIX nanoparticles

and HeLa cells to undergo cellular internalization via endocytosis, which is consistent with the notion that high binding avidity can slow down the penetration of nanocarriers due to a 'binding-site barrier'^[47]. Meanwhile, TPP is a lipophilic molecule with a cationic phosphonium head, which has been demonstrated for mitochondria-targeting delivery of drug payloads. This paper describes for the first time conjugating TPP on the surface of UCNs-PpIX nanoparticles rendering the nanoparticles with the ability to target the mitochondria of HeLa cells, which may be attributed to the substantial negative membrane potential at the mitochondrial inner membrane^[41,42].

Although various approaches to improve ROS generation have been designed, unclear mechanism still remains in the effectiveness of ROS generation on PDT treatment.^[6-16,30-34,48,49] Some studies^[14,16,47-50] reported the relationship between the concentration of nanoparticles or PS and PDT efficacy, but the concentration of nanoparticles or PS is not directly related to the rate or amount of ROS generation. Based on our nanoplatforms, it was possible to study whether the amount of ROS generated affects the capability of killing cancer cells, which has not been reported before. As shown in **Figure 8** and **Figure 9**, we first demonstrated that the dose of ROS does not significantly affect the PDT efficacy, at least in the range investigated in this paper. Since it is difficult to quantitate the amount of nanoplatforms at each specific site, the relationship between the ROS generation and PDT efficacy still needs further investigation based on the quantitative data of local ROS generation.

The influence of ROS generating time on PDT efficacy is of great importance, because the half-life of ¹O₂ is as short as 40 ns, during which the amount of ROS generation may not be sufficient to damage the tumor cells. In our experiments, we found that a 10 min NIR irradiation leads to a certain decrease of cell viability and a prolonged irradiation to more than

30 min results in a further decrease. Our FACS result showed that both mitochondria targeting and cell membrane location show a similar cell death mechanism within 15 min irradiation, but it shows a position-dependent phenomenon when further irradiated for 60 min. This result may be explained by the hypothesis of Nel et. al.^[51] on the mechanism of hierarchical oxidative stress: the lowest level of oxidative stress is associated with the induction of antioxidant and detoxification defense, but at higher levels of oxidative stress, this protective response is overtaken by inflammation and death. The results also showed that after extending irradiation time to 60 min, direct destroy of cell membrane is the main death mechanism for locating nanoparticles on cell membrane, and necrosis or late-stage apoptosis with keeping membrane integrity is dominant for targeting nanoparticles to mitochondria, which indicates that extending ROS generation time leads to different cell responses changing from antioxidant defense to different types of cell death. Contrary to keeping cells integrity, the cell rupture can spread throughout the body for a long time^[52], and despite of the unclear effect^[5], the segments may cause reactions in normal tissues leading to inflammation and edema^[53].

In vitro and *in vivo* studies of the effect of the location of nanoplatform on the PDT efficacy was first performed in this study. Our results showed that the average cell viabilities under the same condition of irradiation for all unmodified UCNs-PpIX nanoparticles (shown in **Figure 6**) were at almost the same level. Meanwhile with or without a washing process, the average cell viabilities under the same condition of irradiation were also at the same level with a very slight decrease. This implies that the ROS generation outside the HeLa cells does not obviously affect the photodynamic efficacy. Previous reports^[17,54,55] also indicated that neat PS outside cells possessed extremely low PDT efficacy despite their capability for high photochemical yield of ROS. Thus, it indicates that ROS localization inside cells is more important than outside. Furthermore, our experimental results first indicate that the viability of HeLa cells treated with FA-modified UCNs-PpIX nanoparticles had a much higher

decrease, ~15%, than those treated with unmodified UCNs-PpIX nanoparticles, and that the HeLa cell viability treated by mitochondria-targeting TPP-modified UCNs-PpIX nanoparticles decreased to ~40%. Previous researches^[54,55] suggested that mitochondrion is the more potent site for PDT than other subcellular sites such as lysosome for cytotoxic activity to living cells. However, those experiments employed different PSs for different locations, so it was difficult to determine the most influential factors of the PDT efficacy: subcellular location, concentration and/or some intrinsic properties. This work was designed to incorporate one sensitizer PpIX for comparison of the influence of cellular location of the nanopatform on PDT efficacy with a similar amount of cellular uptake, and therefore provides direct evidence that the more efficient approach for increasing PDT efficacy is to tailor the nanopatform to target certain subcellular sites such as mitochondria.

4. Conclusion

With the minimization of the external layer thickness and the increase of the loading capacity of PpIX outside a UCN core, the ROS generation rate can be adjusted and controllable. Meanwhile through modifying their surface by targeting ligands of FA and TPP, the UCNs-PpIX nanoparticles can target the cell membrane and mitochondria of HeLa cells, respectively. Based on these newly designed nanopatforms, we found that the mitochondria targeting mode is more significant for the PDT performance of both cell killing (*in vitro*) and tumor growth inhibition (*in vivo*) than the cell membrane mode. The HeLa cells incubated with UCNs-PpIX nanoparticles showed different death mechanisms after 60 min laser exposure: membrane segmentation for membrane targeting, and necrosis or late-stage apoptosis for mitochondria targeting. Moreover, the subcellular position near mitochondria is much more efficient and effective for higher PDT efficacy than increasing ROS generating amount. In summary, we developed novel UCNs-PpIX nanoparticles, which can not only control and optimize ROS generation but also target subcellular-scale organelles. The findings provide

evidence that specific subcellular targeting strategy may be of more importance for optimizing PDT efficacy than elevating the dose of ROS.

Supporting Information

Supporting Information, including experimental section, the UV-Vis absorption for the calculation of PpIX loading and ROS generation, fluorescent spectra, luminescence decay lifetime of different samples, UV-Vis absorption of samples before and after surface modification, and the discussion on ruling out photothermal effect, is available from the Wiley Online Library or from the author.

Acknowledgements

D. Chen and R. Tao contributed equally to this work. This work was financially supported by National Science Foundation of China (Project No. 31100718 and No. 31470958), Shanghai Municipal Science and Technology Commission (Project No. 13441902102), University of Michigan-Shanghai Jiao Tong University Collaboration Fund, and a Global Innovation Initiative (GII) project funded by the British Council and the Department of Business, Innovation and Skills in the United Kingdom. K. T. thanks the support of Science and Technology Cooperation Project of Jiangxi Province (No. 20142BDH80023). We thank Instrumental Analysis Center of SJTU for assistance with the instrumentation.

Received: ((will be filled in by the editorial staff))

Revised: ((will be filled in by the editorial staff))

Published online: ((will be filled in by the editorial staff))

- [1] T. J. Dougherty, G. B. Grindey, R. Fiel, K. R. Weishaupt, D. G. Boyle, *J. Natl. Cancer Inst.* **1975**, *55*, 115-121.
- [2] N. L. Oleinick, R. L. Morris, I. Belichenko, *Photochem. Photobiol. Sci.* **2002**, *1*, 1-21.
- [3] W. M. Sharman, C. M. Allen, J. E. van Lier, *Methods Enzymol.* **2000**, *319*, 376-400.
- [4] A. P. Castano, T. N. Demidova, M. R. Hamblin, *Photodiagn. Photodyn.* **2004**, *1*, 279-293.
- [5] P. Agostinis, K. Berg, K. A. Cengel, T. H. Foster, A. W. Girotti, S. O. Gollnick, S. M. Hahn, M. R. Hamblin, A. Juzeniene, D. Kessel, M. Korbelik, J. Moan, P. Mroz, D. Nowis, J. Piette, B. C. Wilson, J. Golab, *CA Cancer J. Clin.* **2011**, *61*, 250-281.
- [6] S. S. Lucky, K. C. Soo, Y. Zhang, *Chem. Rev.* **2015**, *115*, 1990-2042.
- [7] M. R. Saboktakin, R. M. Tabatabaee, *Int. J. Bio. Macromol.* **2014**, *65*, 398-414.

- [8] D. K. Chatterjee, L. S. Fong, Y. Zhang, *Adv. Drug Deliv. Rev.*, **2008**, *60*, 1627-1637.
- [9] F. Chen, S. Zhang, W. Bu, Y. Chen, Q. Xiao, J. Liu, H. Xing, L. Zhou, W. Peng, J. Shi, *Chem. Euro. J.* **2012**, *18*, 7082-7090.
- [10] N. M. Idris, M. K. Gnanasammandhan, J. Zhang, P. C. Ho, R. Mahendran, Y. Zhang, *Nat. Med.* **2012**, *18*, 1580-1585.
- [11] S. Cui, D. Yin, Y. Chen, Y. Di, H. Chen, Y. Ma, S. Achilefu, Y. Gu, *ACS Nano* **2013**, *7*, 676-688.
- [12] D. Bechet, P. Couleaud, C. Frochot, M. L. Viriot, F. Guillemin, M. Barberi-Heyob, *Trends Biotech.* **2008**, *26*, 612-621.
- [13] C. Wang, L. Cheng, Z. Liu, *Theranostics* **2013**, *3*, 317-330.
- [14] L. Xia, X. Kong, X. Liu, L. Tu, Y. Zhang, Y. Chang, K. Liu, D. Shen, H. Zhao, H. Zhang, *Biomaterials* **2014**, *35*, 4146-4156.
- [15] K. Liu, X. Liu, Q. Zeng, Y. Zhang, L. Tu, T. Liu, X. Kong, Y. Wang, F. Cao, S. A. G. Lambrechts, M. C. G. Aalders, H. Zhang, *ACS Nano* **2012**, *6*, 4054-4062.
- [16] C. Wang, L. Cheng, Y. Liu, X. Wang, X. Ma, Z. Deng, Y. Li, Z. Liu, *Adv. Funct. Mater.* **2013**, *23*, 3077-3086.
- [17] T. J. Dougherty, C. J. Gomer, B. W. Henderson, G. Jori, D. Kessel, M. Korbelik, J. Moan, Q. Peng, *J. Nat. Cancer Ins.* **1998**, *90*, 889-905.
- [18] H. Maeda, J. Wu, T. Sawa, Y. Matsumura, K. Hori, *J. Contr. Release* **2000**, *65*, 271-284.
- [19] J. D. Byrne, T. Betancourt, L. Brannon-Peppas, *Adv. Drug Deliv. Rev.* **2008**, *60*, 1615-1626.
- [20] Li, C., *Nat. Mater.* **2014**, *13*, 110-115.
- [21] V. P. Torchilin, *Ann. Rev. Biomed. Eng.* **2006**, *8*, 343-375.
- [22] D. Putnam, *Nat. Mater.* **2006**, *5*, 439-451.
- [23] S. Biswas, V. P. Torchilin, *Adv. Drug Deliv. Rev.* **2014**, *66*, 26-41.

- [24] S. Biswas, N. S. Dodwadkar, R. R. Sawant, A. Koshkaryev, V. P. Torchilin, *J. Drug Targeting* **2011**, *19*, 552-561.
- [25] L. E. Samuelson, M. J. Dukes, C. R. Hunt, J. D. Casey, D. J. Bornhop, *Bioconj. Chem.* **2009**, *20*, 2082-2089.
- [26] G. Sahay, V. Gautam, R. Luxenhofer, A. V. Kabanov, *Biomaterials* **2010**, *31*, 1757-1764.
- [27] R. Thekkedath, A. Koshkaryev, V. P. Torchilin, *Nanomedicine* **2012**, *8*, 1-11.
- [28] H. Akita, A. Kudo, A. Minoura, M. Yamaguti, I. A. Khalil, R. Moriguchi, T. Masuda, R. Danev, K. Nagayama, K. Kogure, H. Harashima, *Biomaterials* **2009**, *30*, 2940-2949.
- [29] H. Sneh-Edri, D. Likhtenshtein, D. Stepensky, *Mol. Pharma.* **2011**, *8*, 1266-1275.
- [30] D. K. Chatterjee, Y. Zhang, *Nanomedicine* **2008**, *3*, 73-82.
- [31] P. Zhang, W. Steelant, M. Kumar, M. Scholfield, *J. Am. Chem. Soc.* **2007**, *129*, 4526-4527.
- [32] H. S. Qian, H. C. Guo, P. C. L. Ho, R. Mahendran, Y. Zhang, *Small* **2009**, *5*, 2285-2290.
- [33] A. Master, M. Livingston, A. Sen Gupta, *J. Contr. Release* **2013**, *168*, 88-102.
- [34] Z. Zhao, Y. Han, C. Lin, D. Hu, F. Wang, X. Chen, Z. Chen, N. Zheng, *Chem. Asian J.* **2012**, *7*, 830-837.
- [35] L. M. Rossi, P. R. Silva, L. L. R. Vono, A. U. Fernandes, D. B. Tada, M. S. Baptista, *Langmuir* **2008**, *24*, 12534-12538
- [36] M. I. Souza, Y. M. Jaques, G. P. De Andrade, A. O. Ribeiro, E. R. Da Silva, E. E. Fileti, E. D. S. Ávilla, M. V. B. Pinheiro, K. Krambrock, W. A. Alves, *J. Phys. Chem. B* **2013**, *117*, 2605-2614.
- [37] A. Scomparin, S. Salmaso, S. Bersani, R. Satchi-Fainaro, P. Caliceti, *Euro. J. Pharm. Sci.* **2011**, *42*, 547-558.
- [38] M. Wojtoniszak, D. Roginska, B. Machalinski, M. Drozdik, E. Mijowska, *Mater. Res. Bull.* **2013**, *48*, 2636-2639.

- [39] T. Tree-Udom, P. Thamyongkit, N. Wiratkasem, C. Chanchao, T. Palaga, N. Insin, S. Rengpipat, P. Pienpinijtham, S. Wanichwecharungruang, *RSC Adv.* **2015**, *5*, 102416-102423.
- [40] F. Moret, D. Scheglmann, E. Reddi, *Photochem. Photobio. Sci.* **2013**, *12*, 823-834.
- [41] R. A. J. Smith, C. M. Porteous, A. M. Gane, M. P. Murphy, *Proc. Nat. Acad. Sci. USA* **2003**, *100*, 5407-5412.
- [42] S. Marrache, S. Dhar, *Proc. Nat. Acad. Sci. USA* **2012**, *109*, 16288-16293.
- [43] E. M. M. Manders, F. V. Verbeek, J. A. Aten, *J. Microscopy* **1993**, *169*, 375-382.
- [44] Z. Darzynkiewicz, S. Bruno, G. Del Bino, W. Gorczyca, M. A. Hotz, P. Lassota, F. Traganos, *Cytometry* **1992**, *13*, 795-808.
- [45] K. E. Sapsford, L. Berti, I. L. Medintz, *Angew. Chem. Inter. Ed.* **2006**, *45*, 4562-4588.
- [46] I. L. Medintz, H. Mattoussi, *Phys. Chem. Chem. Phys.* **2009**, *11*, 17-45.
- [47] D. Peer, J. M. Karp, S. Hong, O. C. Farokhzad, R. Margalit, R. Langer, *Nat. Nanotech.* **2007**, *2*, 751-760.
- [48] M. Wang, Z. Chen, W. Zheng, H. Zhu, S. Lu, E. Ma, D. Tu, S. Zhou, M. Huang, X. Chen, *Nanoscale* **2014**, *6*, 8274-8282.
- [49] S. Cui, H. Chen, H. Zhu, J. Tian, X. Chi, Z. Qian, S. Achilefu, Y. Gu, *J. Mater. Chem.* **2012**, *22*, 4861-4873.
- [50] J. Moan, *Photochem. Photobio.* **1986**, *43*, 681-690.
- [51] A. Nel, T. Xia, L. Mädler, N. Li, *Science* **2006**, *311*, 622-627.
- [52] S. Y. Proskuryakov, A. G. Konoplyannikov, V. L. Gabai, *Exp. Cell Res.* **2003**, *283*, 1-16.
- [53] S. Elmore, *Toxicol. Pathol.* **2007**, *35*, 495-516.
- [54] E. Buytaert, M. Dewaele, P. Agostinis, *Biochim. Biophys. Acta. Rev. Cancer* **2007**, *1776*, 86-107.
- [55] D. Kessel, Y. Luo, Y. Deng, C. K. Chang, *Photochem. Photobio.* **1997**, *65*, 422-426.

Figure 1. Schematic illustration of modified microemulsion approaches for coating silica and PS on upconversion nanoparticles. The inset table shows the feeding and loading amounts of PpIX molecules for each sample and their energy transfer efficiency calculated from fluorescent intensity.

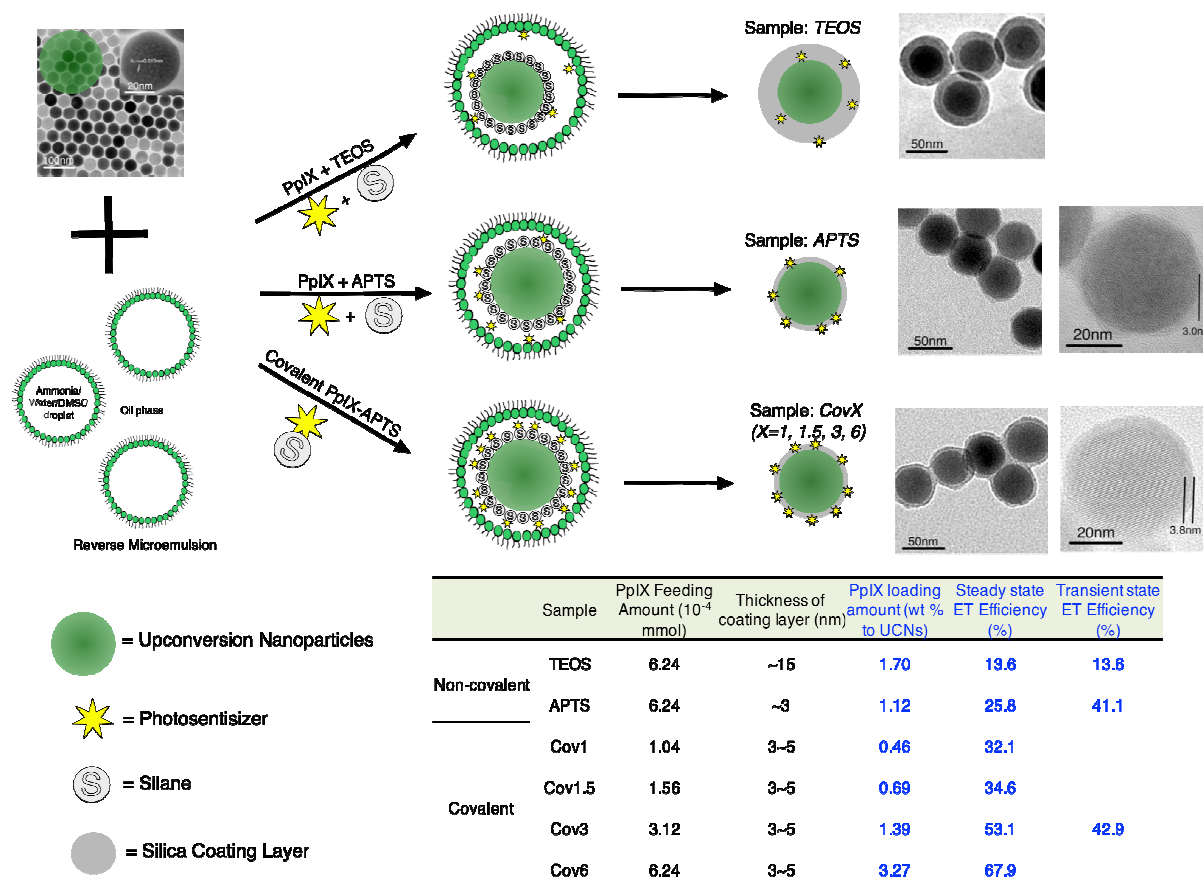
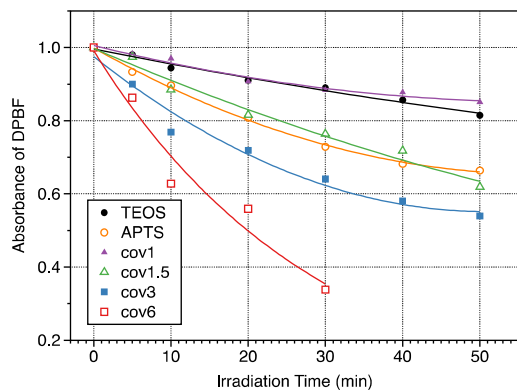
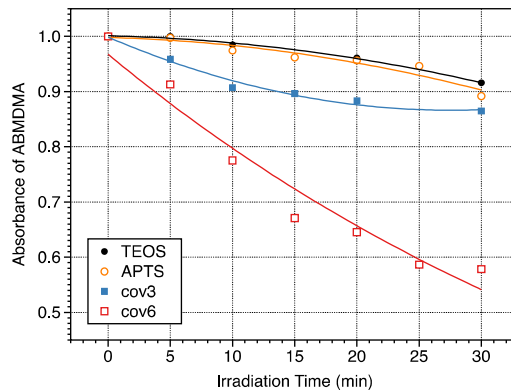


Figure 2. (a) The ROS generation of different samples as indicated by the decay of absorbance of DPBF at 410 nm, and (b) the $^1\text{O}_2$ generation of different samples as indicated by the decay of absorbance of ABMDMA



(a)



(b)

Figure 3. Right Panel: Schematic illustration of UCNs-PpIX nanoparticles surface modification with folic acid (FA) and (3-carboxypropyl)triphenylphosphonium bromide (TPP), respectively. Two-photon confocal fluorescent microscopic images of HeLa cells incubated with different surface modified Cov6 samples. Each series can be classified into the nuclei of cells (being dyed in blue by DAPI for visualization), PpIX-loaded upconversion nanoparticles, and a combination of both channels, respectively. The light source was a 980 nm pulse laser. Left panel: Cellular uptake of different surface modified nanoparticles.

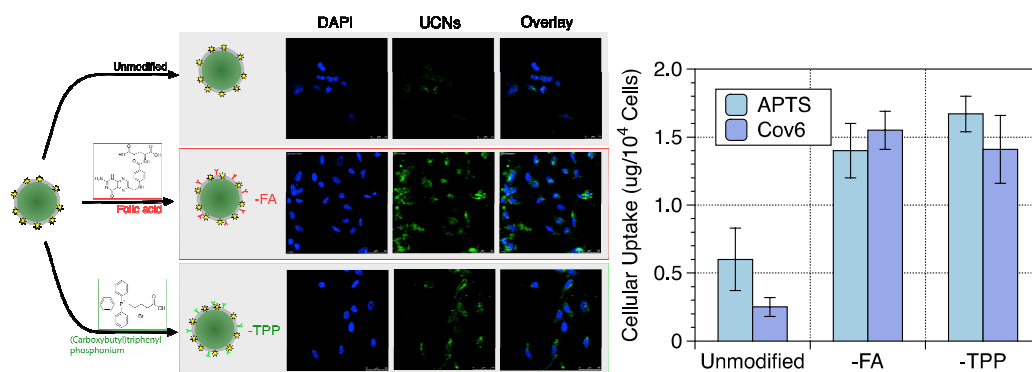


Figure 4. TEM images of HeLa cells incubated with different surface modified Cov6 samples, showing different targeting positions: Unmodified, FA modified and TPP modified sample Cov6 for untargeted, membrane targeted and near mitochondria location, respectively. Arrows point to the aggregation of ROS generation nanoplatforms.

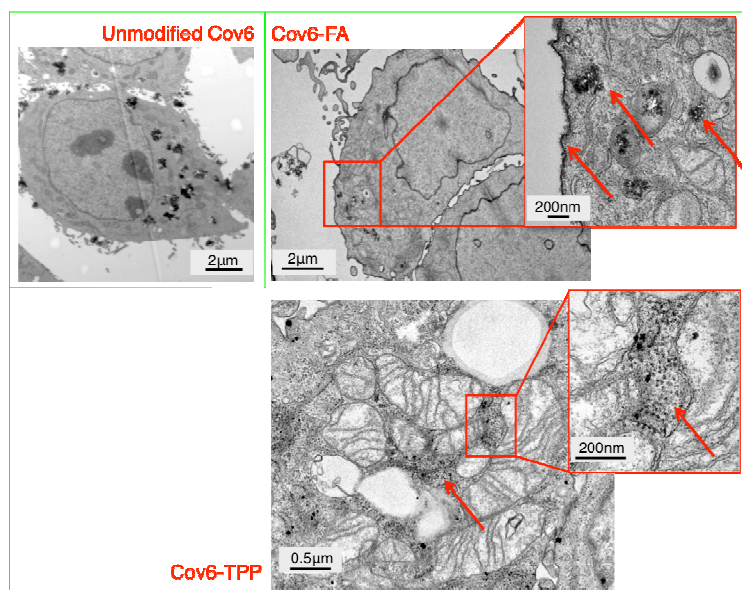


Figure 5. Multichannel confocal fluorescence micrographs. Blue channel ($\lambda_{\text{ex}}=385$ nm, $\lambda_{\text{em}}=470$ nm) for DAPI stained nuclei. Red channel ($\lambda_{\text{ex}}=552$ nm, $\lambda_{\text{em}}=660$ nm) for PpIX. Green channel ($\lambda_{\text{ex}}=488$ nm, $\lambda_{\text{em}}=530$ nm) for Rh123 stained mitochondria.

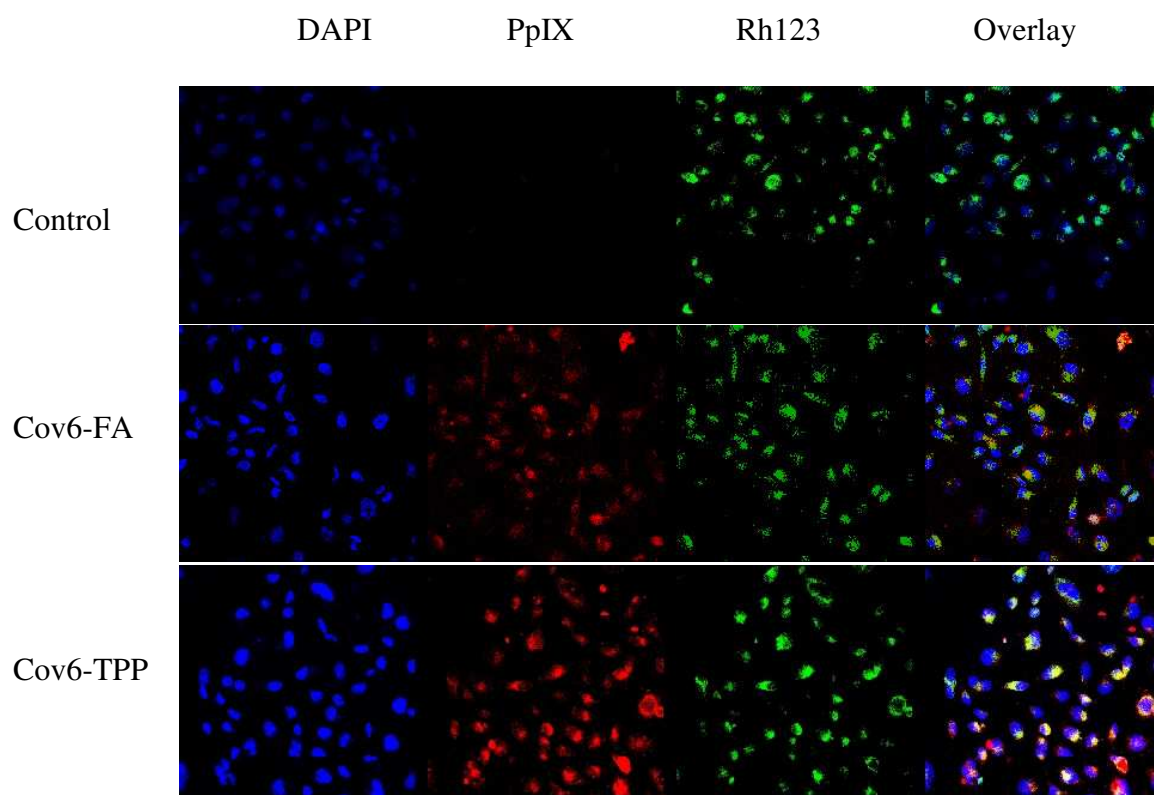


Figure 6. The viability of HeLa cells incubated with unmodified samples in dark, or under 980 nm irradiation with/without washing off the UCNs-PpIX nanoparticles outside cells.

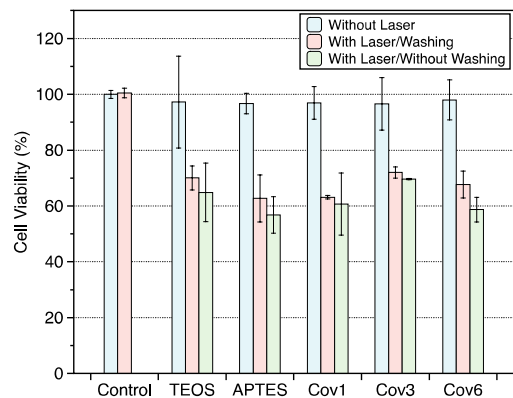


Figure 7. The viability of HeLa cells incubated with different surface modified Cov6 samples after irradiation for various periods of time with a 980 nm NIR laser.

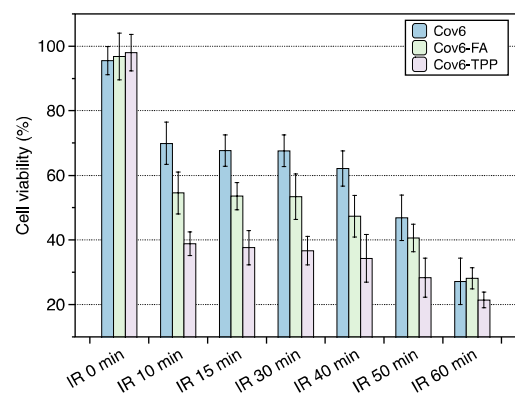


Figure 8. Cytotoxicity of cells incubated with FA-modified samples exposing to 0~60 min NIR irradiation.

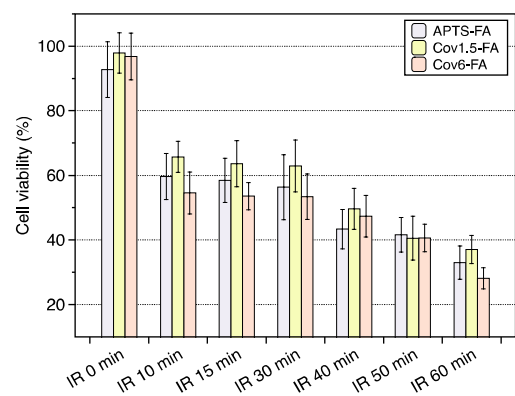


Figure 9. The viability of HeLa cells incubated with samples APTS and Cov6 with different surface modifications in dark, and under 15 min and 40 min irradiations, respectively.

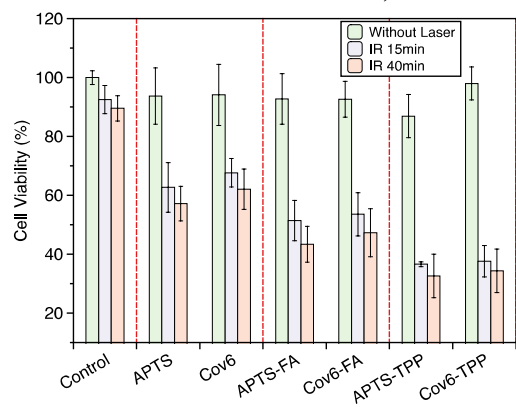


Figure 10. Fluorescein annexin-V-FITC/PI double labeling flow cytometry results for HeLa cells incubated with samples Cov6-FA and Cov6-TPP in dark and under 15 min and 60 min irradiations, respectively.

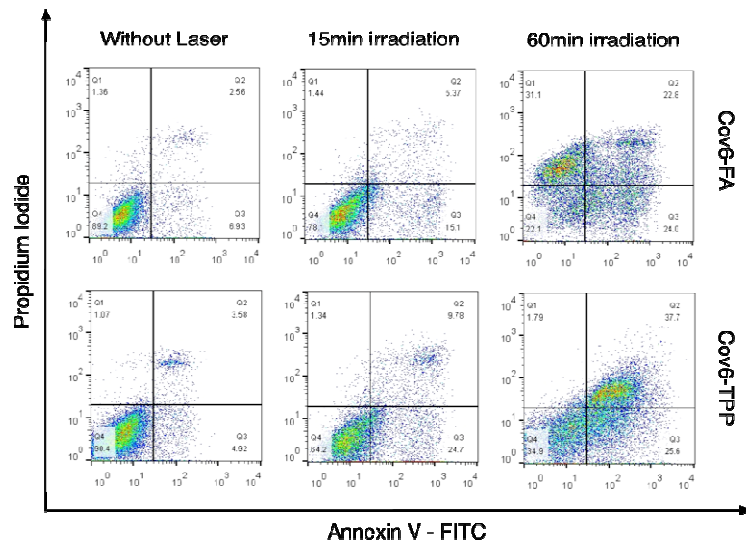


Figure 11. (a) The photograph of the tumor in a mouse exposed to 980 nm laser, showing the upconversion fluorescence of UCNs-PpIX nanoparticles; (b) the evolution of tumor size under different treatments, in which the red arrow shows that the laser irradiation was implemented on the first and second day for 30 min in each day; (c) The photograph of the tumor size evolution from day 0 to day 12. Scale bar is 1 cm.

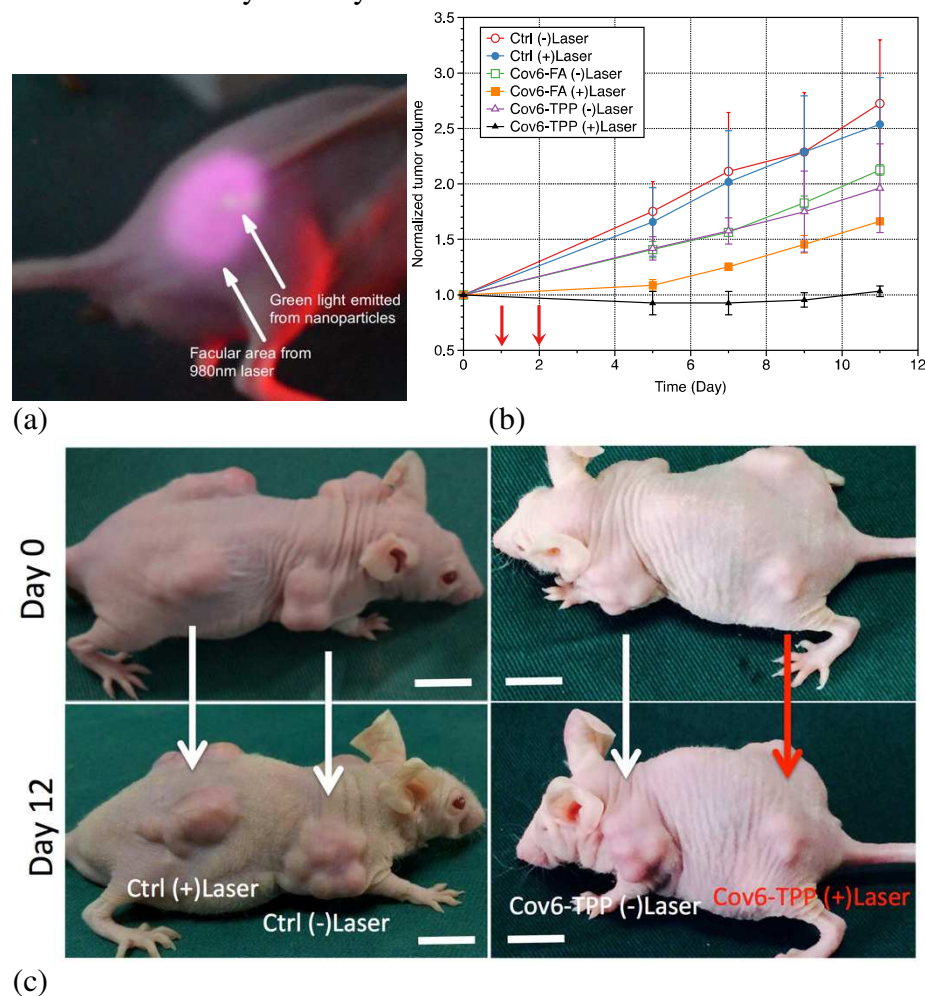


Figure 12. Hematoxylin & Eosin (H&E) stained tumor tissues harvested from the mice with different treatments after 12 days. The 3rd and 5th Columns are the fluorescent microscopic observation of the corresponding samples of the 2nd and 4th Columns, respectively.

